

Phase-matched electron-photon interactions enabled by 3D-printed helical waveguides

Masoud Taleb,¹ Mohsen Samadi,² and Nahid Talebi^{1,*}

¹Institute of Experimental and Applied Physics, Kiel University, 24098 Kiel, Germany

²Department of Electrical and Information Engineering, Kiel University, 24143 Kiel, Germany

ABSTRACT. The Smith-Purcell effect enables electromagnetic radiation across arbitrary spectral ranges by phase-matching the diffraction orders of an optical grating with the near-field of a moving electron. In this work, we introduce a novel approach using a helically shaped waveguide, where phase-matching is achieved through guided light within a helical optical fiber fabricated via two-photon polymerization using a 3D printer. Our results demonstrate that radiation from these structures precisely satisfies the phase-matching condition and is emitted directionally at specific angles, contrasting with the broad angular distribution characteristic of the traditional Smith-Purcell effect. Helical electron-driven photon sources establish a new paradigm, enabling 3D-printed structures to control electron-beam-induced radiation and, inversely, to facilitate light-induced efficient electron beam shaping and acceleration.

Electron-driven photon sources are electromagnetic radiation sources integrated into electron microscopes as internal emitters [1-4], with applications in spectral interferometry [5,6] and time-resolved spectroscopy [7]. These sources typically consist of nanostructured metallic planar films that in interaction with electron beams generate light with specific radiation profiles, such as focused radiation [1] or vortex beams [8,9]. While they provide a versatile platform for generating shaped electromagnetic radiation at specific photon energies defined by surface plasmon resonances, their relatively weak radiation intensities limit their effectiveness in nonlinear optics and pump-probe spectroscopy applications.

Hence, other radiation mechanisms from electron beams could be utilized to enhance the radiation intensity, particularly through phase-matching (synchronization) between the near-field of the moving electron and the induced polarizations in the material [10-15]. Cherenkov radiation [16] and Smith-Purcell effect [17] are among radiation mechanisms enabled by phase-matching.

Cherenkov radiation is the radiation caused by electron beams travelling in a medium where the phase velocity of light is larger than the electron group velocity. Cherenkov radiation forms a light cone along the electron trajectory, with the cone angle θ specified by the phase-matching condition $nk_0 \cos \theta = \omega v_e^{-1}$, resulting in $\cos \theta = c(nv_e)^{-1}$ [3,18]. Here, k_0 is the radiation wavenumber, ω is its angular frequency, and v_e is the electron's group velocity. This criterion however, neglects the fact that electron beams cannot

propagate for long distances in materials, due to the strong elastic and inelastic scatterings from atoms and material excitations. Instead, electron beams travelling in vacuum near a vacuum/material interface and parallel to it provide an alternative [19,20]. When the Cherenkov radiation is coupled to a waveguide mode copropagating with the electron, it leads to a strong, resonant, and phase-matched electron-photon interaction [21,22]. However, the Cherenkov radiation in this case remains in the waveguide, making it inaccessible for far-field detectors.

Smith-Purcell effect mediates electron-photon interactions via coupling to optical grating modes, with a discrete set of wave numbers as $k_m = k_0 \cos \theta + 2m\pi\Lambda^{-1}$, associated with optical rays propagating in various directions in vacuum [23-25]. Here, Λ is the grating period and m is an integer, defining the diffraction mode. The phase-matching scenario in this case is recast as $k_m = \omega v_e^{-1}$.

With the aim of combining these two mechanisms of radiation, a 3D-printed helical waveguide is proposed and explored here (Fig. 1(a)). The waveguide is composed of a polymer resin with the radius of 400 nm, where a thin layer of metal, with the thickness of approximately 40 nm, is deposited on it. The helix is fabricated using two-photon polymerization [26-31] in a Nanoscribe Quantum X system with a 63x NA1.4 objective and an IP-Dip 2 resin with the refractive index of $n_{\text{pol}} = 1.55$. The radius of the helix, measured as the distance between the center of the waveguide to helix axis, is $r_h = 1.76 \mu\text{m}$, and the helical pitch is $\Lambda = 5.85 \mu\text{m}$. For simplicity, we assume that the waveguiding modes

*Contact author: talebi@physik.uni-kiel.de; ORCID: 0000-0002-3861-1005

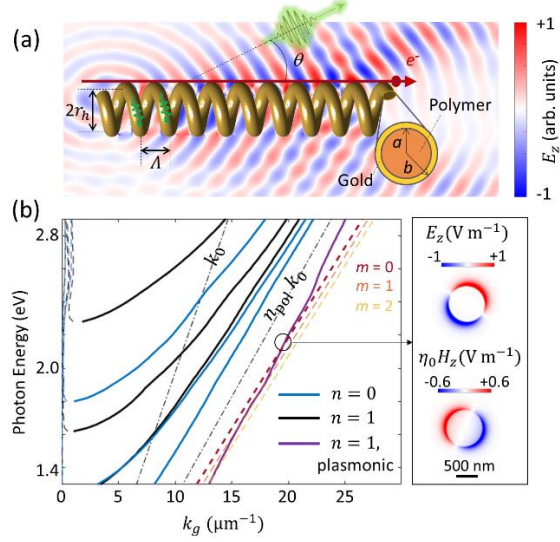


FIG 1. Phase-matched generation of Smith-Purcell radiation from a helical waveguide. (a) Topology of the structure, where a moving electron travels parallel with the screw axis of a helix. The helix is composed of a polymer fiber with a radius of $a = 400$ nm and with a 40 nm gold layer deposited on it. (b) Left: Calculated dispersion of the fiber modes. The dashed-dotted lines indicate the light lines in vacuum and fiber. Thin dashed lines show the attenuation constant and thick solid lines the phase constant. The red, orange, and yellow dashed lines specify the phase matching condition corresponding to a moving electron at the kinetic energy of 18 keV (Eq. (1) in the text). Right: Spatial profiles of the z -component of the electric and magnetic fields at the depicted point.

remain unchanged when the straight fiber is transformed into a helix. The waveguide dispersion can be solved analytically (Fig. 1(b); see Supplementary Note 1 for the solutions [32]). The modes of waveguides with cylindrical symmetries are generally decomposed versus the azimuthal order n , ranging from $n = 0$ (no azimuthal dependence; shown by blue lines in Fig. 1(b)) to higher order modes with $n \geq 1$ (shown by black and purple lines). The latter are hybrid in nature, i.e., they are in the form of the supersposition of TE_z (transverse electric to z) and TM_z (transverse magnetic to z). The fundamental mode of the waveguide is also a hybrid mode with $n = 1$ (purple line in Fig. 1(b)), lying outside the light line in polymer. This mode has a plasmonic nature, with its field being tightly confined to the thin metallic region (Fig. 1(b), right).

A moving electron propagating parallel to the helix axis at a distance of $r_h + b + 20$ nm, therefore not travelling through the matter, can excite the propagating modes of the waveguide. Sequential interaction of the electron with the waveguide at each

turning point of the helix, leads to sequential photon emissions into the guided modes. In the case of the constructive interaction, the phase-matching condition leads to $k_g \sqrt{(2\pi r_h)^2 + \Lambda^2} + 2m\pi = \Lambda \omega / v_e$ with k_g being the phase constant of the optical modes of the fiber. This condition is recast in the form of

$$k_g = (\Lambda \omega / v_e - 2m\pi) \cdot \left((2\pi r_h)^2 + \Lambda^2 \right)^{-\frac{1}{2}}. \quad (1)$$

The right side of Eq. (1) is provided as red, orange and yellow dashed lines in Fig. 1(b), for an electron at the kinetic energy of 18 keV, and with $m = 0, 1$, and 2 , respectively. Electrons having a kinetic energy (U_{el}) in the range of $16 \text{ keV} \leq U_{el} \leq 20 \text{ keV}$ are able to couple to the plasmonic mode in a phase-matched condition with $m = 0$, whereas coupling to this mode for higher electron energies is only possible by higher diffraction orders, namely $m > 0$. The metallic layer serves a dual purpose in our configuration: it facilitates the coherent excitation of plasmonic waves and their interaction with electron beams, while also preventing charging of the helix under electron beam irradiation. This merged Cherenkov and Smith-Purcell emission mechanism significantly enhances the radiation. The emitted photons constitute a rate of approximately 0.02 photon per given electron (for a Helix with 11 turns), significantly higher than the emission from planar, plasmonic-based electron-driven photon sources emitting at the rate of approximately 10^{-4} per given electron, as confirmed by our measurements presented below.

The helical waveguides are positioned on top of a plateau fabricated at the same size of the helices (Fig. 2(a) and (b) and supplementary Figure S1). The structures are held by a special SEM holder fabricated for precise alignment with respect to the electron beam, therefore the electron travels parallel with the helix axis (See supplementary Figure S1). For measuring the radiation from electron beams interacting with the helical waveguide, a DELMIC SPARC cathodoluminescence (CL) spectroscopy and angle-resolve mapping system installed in a ZEISS SIGMA scanning electron microscope is used (Fig. S1). A parabolic mirror positioned either above or below the helix gathers the radiation with the collection angular range of 1.46π sr, and collimates it toward the analyzing path [33]. For the measurements shown below an electron beam at the kinetic energy of 18 keV and the current of 10 nA is used and the mirror is positioned below the helix.

Figure 2(c) shows the CL spectrum as a function of the electron impact position, varying from 320 nm

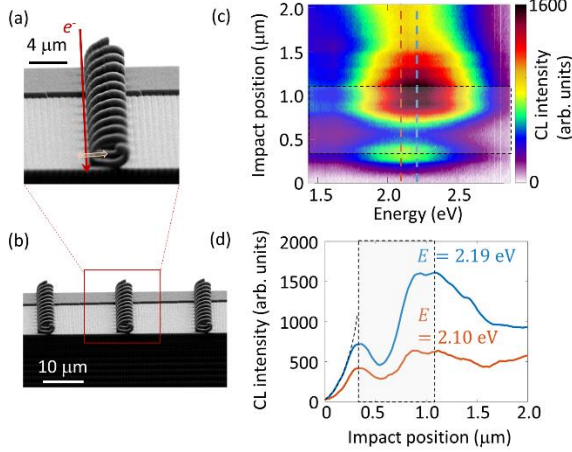


FIG 2. 3D-printed helical waveguide. (a) secondary electron image of a single 3D-printed helical waveguide. (b) SE image of a series of such waveguides arranged on a plateau. (c) CL spectra as a function of the electron impact position along the path indicated by the arrow in (a). The region within the core of the helical waveguide and its metallic shell is highlighted with a dashed, shaded box. (d) Linear plots of the CL intensity versus electron impact position at the specified photon energies.

away from the waveguide rim toward the helical axis until a distance of 500 nm from the axis. The intensity reaches a maximum at the photon energy of 2.1 eV at the rim of the waveguide and exhibits an evanescent decay with a decay length of 120 nm (Fig. 2(d)). The emitted photon energy perfectly matches the phase-matching criterion explained by equation (1) and demonstrated in Fig. 1(b). Within the helical arm, the CL intensity also shows an evanescent tail, decreasing to a minimum at a distance of 185 nm from the rim and increasing again towards the opposite rim. At this opposing rim, located at a position $1.2\mu\text{m}$ from the origin, the intensity is higher, creating a double-peak feature. This double-peak behavior is attributed to a slight misalignment of the helix, causing it to deviate from being perfectly parallel to the beam trajectory (Fig. S1). The maximum CL intensities observed at the waveguide rims confirm the efficient coupling of the electron beam to the plasmonic mode.

The CL intensity remains at 60% of its maximum amplitude at the helix center, where the electron beam does not interact directly with the material and is approximately $1.3\mu\text{m}$ away from the waveguide rim. The asymmetrical coupling to the plasmonic modes at the opposing rims, combined with the higher CL intensity observed when the electron travels through the axial void, indicates a significant coupling of the evanescent tails of the plasmonic fields within the axial void. The resulting modal structure facilitates efficient electron-photon interactions, even in regions

where the electron is $1\mu\text{m}$ away from the rim of the waveguide.

To further illustrate the angular range of the emission, the CL emission is resolved versus the polar angle of the emission and photon energy, by performing momentum-resolved spectroscopy (Fig. 3(a) and (b)) [34]. The azimuthal angle is restricted to angular range along which the maximum emission is observed; i.e., $\varphi = \pm 10^\circ$, where the latter is confirmed by angle-resolved mapping shown further below (Fig. 3(c)).

The angle-resolved spectral CL map displays a broad peak at the energy of 2.1 eV to 2.5 eV, collimated along the symmetry axis of the grating. The dark regions at $\theta = 0$ and at $\theta > 80^\circ$ correspond to the hole implemented into the mirror for avoiding electron beam contamination and damage, and the restricted collection efficiency of the mirror due to its limited size, respectively. This collimated emission and its photon energy agrees well with the $m = 0$ emission (dashed red line in Fig. 1(b)). The higher-order diffraction orders are obvious as well with faint directional emissions at higher angles, marked by dashed orange ($m = 1$) and dashed yellow ($m = 2$) lines in Fig. 3(b).

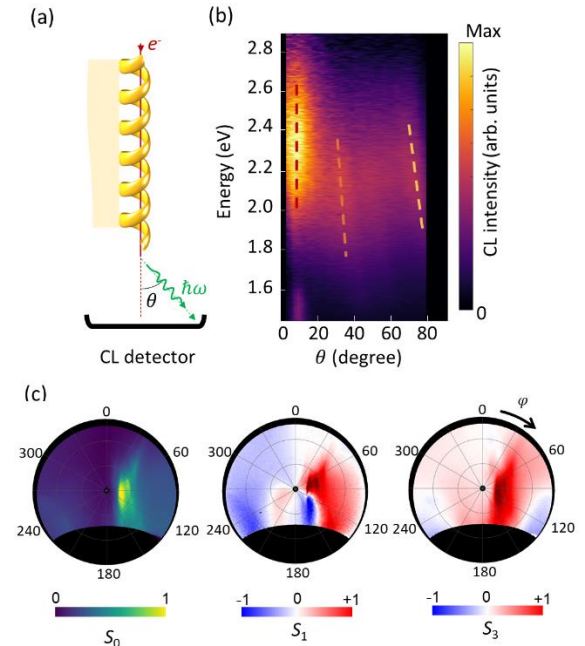


FIG. 3. (a) The schematic of the experiment. (b) Angle-resolved CL spectra, and (c) angle-resolved stokes parameters of the radiation measured at the integrated photon energy range of 2.15 eV to 2.26 eV. Electron beam has the kinetic energy of 18 keV and propagates parallel to the helix axis at the impact position of $r_h + b + 20\text{ nm}$, forming a spot size of 100 nm.

The interaction of the electron beam with the chiral helix induces a chiral current inside the lattice, that forms an elliptically-polarized light. The excitation of the electron beam parallel to the helix axis leads to a chiral polarization following the helicity of the structure. The emission profile therefore follows as well the handedness of the helix, in such a way that the emission is predominantly in the form of right-handed circularly polarized light, where the detector convention is considered. Measured Stokes parameters, namely $S_0 = |A_x|^2 + |A_y|^2$ (light intensity), $S_1 = |A_x|^2 - |A_y|^2$, and $S_3 = 2\text{Im}\{A_x^*A_y\}$ verify the generation of directional and right-handed circularly-polarized light (Fig. 3(c)). In the above equations, A_x and A_y depict the complex amplitudes of the x - and y - components of the electric field. For an elliptically-polarized light, where a phase offset exists between A_x and A_y components, S_3 takes a non-zero value and its sign is associated with the handedness of the polarization (positive for right-handed and negative for left-handed polarization, when the detector convention is used).

To further demonstrate that the radiation originates from the combined Cherenkov and Smith-Purcell emission mechanism described by Eq. (1), we have performed angle-resolved spectroscopy and polarimetry measurements for the case where the electron beam traverses the helix perpendicular to its axis (Fig. 4). In this configuration, the emission exhibits a distinct profile, peaking at 1.6 eV and extending toward higher angular ranges. The emitted photon energy in this case does not depend on the electron impact position. Since the helix is long, reflections from its ends are negligible, preventing the formation of standing-wave patterns within the helix. This indicates that the electron primarily couples to lower-energy modes of the waveguide, which emit from the waveguide's ends, resulting in a broad angular distribution.

Polarimetry measurements further reveal significant differences in polarization between emissions from the two ends of the waveguide. The left end predominantly emits right-handed polarized light, while the right end emits left-handed polarized light. These results align with observations reported elsewhere and can be attributed to the dependence of the emission's chirality on the electron beam's impact position [35].

Noticeably, the emission from the helix in the case when electron travels parallel to the helix axis, cannot be described by Smith-Purcell radiation. There is a large mismatch between the momentum of the free-space light and the momentum of the current-density

distribution of the moving electron at the kinetic energy of 18 keV. Therefore, to satisfy the Smith-Purcell criterion, namely, $\omega v_e^{-1} = k_0 \cos \theta + 2m\pi\Lambda^{-1}$, diffraction orders of $13 \leq m \leq 35$ is required, for the photon energy within 1 eV and 3 eV, which makes the interaction rather inefficient.

The simulations of a moving electron interacting with the helix reproduce the main observed features. These simulations were performed using a finite-difference time-domain (FDTD) solver developed in our group [36]. The large size of the structure, combined with its fine features (e.g., the gold layer thickness and confined plasmon polaritons), posed significant computational challenges. We discretised the entire volume using a 15 nm grid size and introduced 20000 time iterations. A second-order radiation boundary condition was employed to eliminate the need for additional volume required by perfectly matched layers. The calculated spectrum of the light intensity (Poynting vector) at surface positioned 8 μm below the helix demonstrates a broad resonance centered at $E = 2.2$ eV in a good agreement with observed experimental results. The emission from the helix is also collimated downward, making an angle of approximately 20 degrees with the electron beam trajectory. The transverse field intensity

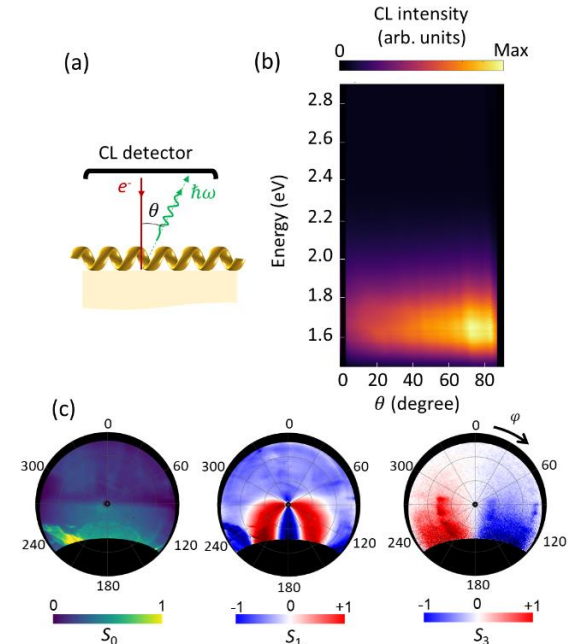


FIG. 4. (a) Schematic of the experiment. (b) Angle-resolved CL spectra and (c) angle-resolved Stokes parameters of the radiation measured at the integrated photon energy range of 1.6 eV to 1.7 eV. The electron beam has the kinetic energy of 18 keV and propagates perpendicular to the helix axis.

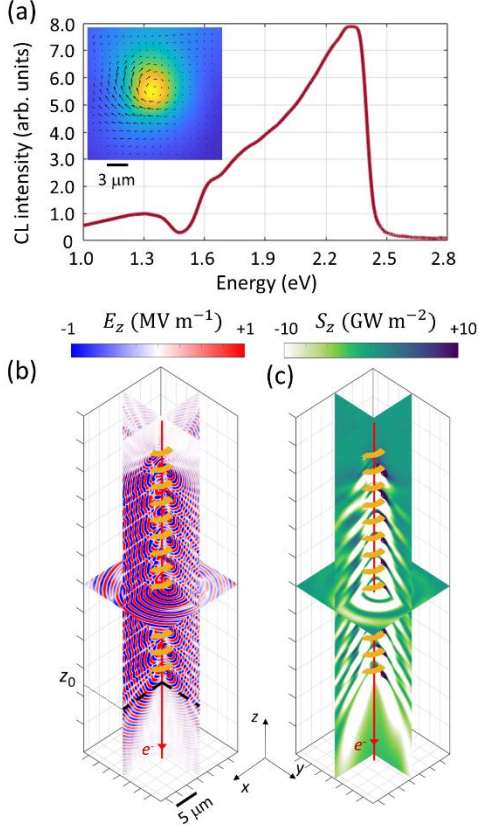


FIG. 5. Simulation results, exhibiting the interaction of a moving electron at the kinetic energy of 18 eV interacting with the helix. The inset shows the spatial profile of the z -component of the electric field at $z = z_0$. The inset displays the spatial profile of absolute value of the transverse electric field at the xy -plane marked by z_0 , positioned at $3\mu\text{m}$ below the helix end. (a) Radiation spectrum, calculated at the xy -plane positioned at $8\mu\text{m}$ below the helix. The spatial profile of the (b) z -component of the electric field and (c) the z -component of the Poynting vector, at $E = 2.22\mu\text{m}$.

$(|E_x|^2 + |E_y|^2)$ has a collimated spatial profile and constitutes an elliptical polarization (Inset of Fig. 5(a)). The field profiles are symmetrical distributed with respect to the helix axis, in contrast with the experiments, due to the presence of the plateau in the latter that is required to hold the helix.

Similar to the Cherenkov radiation and the Smith-Purcell effect, the energy of the emitted photons can be tuned via the electron kinetic energy. Supplementary Note S3 and Fig. S2 indicate that this indeed can be observed as a control parameter.

Based on comparisons between the experimental results and the phase-matching condition—where the

phase constant of the optical modes is assumed to correspond to that of a straight optical fiber—we conclude that the optical modes are only slightly modified by transforming the waveguide into a helical structure. This is justified by the relatively large helical pitch of the helix compared to the fiber's radius, which supports this assumption.

Finally, helical structures have previously been proposed to generate helically shaped optical wavefronts. However, our helical waveguide takes advantage of the guided modes of a 3D-printed waveguide to generate phase-matched radiation from electron beams in the visible range, unlike the generation of terahertz Smith-Purcell radiation [37-39].

In conclusion, we have established a new phase-matching scenario that enables stronger electron-photon interactions. This is achieved by maintaining synchronicity between the waveguiding modes of an optical fiber made into a helix and electron beams through the introduction of extended optical paths and multiple sequential interactions. The structure is fabricated using two-photon-polymerization-based 3D printers (Quantum X series, NanoScribe Company), enabling a new paradigm for strong electron-photon interactions. Our phase-matching scenario could be modified for even stronger interactions, e. g., by inserting the helix in a hollow cylindrical waveguide. In an inverse approach [40-42], launching optical waves into the fiber and leveraging laser-induced near-field interactions could enable regimes of ultra-strong electron-photon interactions, which are highly favorable for dielectric laser accelerators.

ACKNOWLEDGMENTS

We acknowledge collaborations with Dr. Jochen Zimmer, Mr. Fabian Rahn and Dr. Aaron Kobler for fabricating the structures (NanoScribe Company). This project has received funding from the Volkswagen Foundation (Momentum Grant), European Research Council (ERC) under the European Union's Horizon 2020 research and innovation program under grant agreement no. 802130 (Kiel, NanoBeam) and grant agreement no. 101017720 (EBEAM), and from Deutsche Forschungsgemeinschaft.

- [1] N. Talebi, S. Meuret, S. Guo, M. Hentschel, A. Polman, H. Giessen, and P. A. van Aken, *Nature Communications* **10**, 599 (2019).
- [2] J. Christopher, M. Taleb, A. Maity, M. Hentschel, H. Giessen, and N. Talebi, *Nanophotonics* **9**, 4381 (2020).
- [3] N. Talebi, *Journal of Optics* **19**, 103001 (2017).
- [4] G. Adamo, K. F. MacDonald, Y. H. Fu, C. M. Wang, D. P. Tsai, F. J. García de Abajo, and N. I. Zheludev, *Physical Review Letters* **103**, 113901 (2009).
- [5] N. Talebi, *Scientific Reports* **6**, 33874 (2016).
- [6] M. Taleb, M. Hentschel, K. Rossnagel, H. Giessen, and N. Talebi, *Nature Physics* **19**, 869 (2023).
- [7] P. B. Masoud Taleb, Mximilian Black, Mario Hentschel, Wilfried Sigle, Benedikt Haas, Christoph Koch, Peter A. van Aken, Harald Giessen, Nahid Talebi, arXiv:2404.09879 (2024).
- [8] N. van Nielen, M. Hentschel, N. Schilder, H. Giessen, A. Polman, and N. Talebi, *Nano Letters* **20**, 5975 (2020).
- [9] G. Li, B. P. Clarke, J.-K. So, K. F. MacDonald, and N. I. Zheludev, *Nature Communications* **7**, 13705 (2016).
- [10] N. Talebi, W. Sigle, R. Vogelgesang, M. Esmann, S. F. Becker, C. Lienau, and P. A. van Aken, *ACS Nano* **9**, 7641 (2015).
- [11] J. McNeur *et al.*, *Optica* **5**, 687 (2018).
- [12] L. Zhang, H. Xu, and W. Liu, *Physical Review Accelerators and Beams* **27**, 110401 (2024).
- [13] A. Feist *et al.*, *Science* **377**, 777 (2022).
- [14] R. Dahan *et al.*, *Nature Physics* **16**, 1123 (2020).
- [15] O. Kfir, H. Lourenço-Martins, G. Storeck, M. Siviš, T. R. Harvey, T. J. Kippenberg, A. Feist, and C. Ropers, *Nature* **582**, 46 (2020).
- [16] I. M. Frank, *Soviet Physics Uspekhi* **27**, 385 (1984).
- [17] S. J. Smith and E. M. Purcell, *Physical Review* **92**, 1069 (1953).
- [18] F. J. García de Abajo, *Reviews of Modern Physics* **82**, 209 (2010).
- [19] Y. Adiv *et al.*, *Physical Review X* **13**, 011002 (2023).
- [20] F. J. García de Abajo, A. Rivacoba, N. Zabala, and N. Yamamoto, *Physical Review B* **69**, 155420 (2004).
- [21] Z. C. Zetao Xie, Hao Li, Qinghui Yan, Hongsheng Chen, Xiao Lin, Ido Kaminer, Owen D. Miller, Yi Yang, arXiv:2404.00377 (2024).
- [22] N. Talebi, *New Journal of Physics* **16**, 053021 (2014).
- [23] Y. J. Tan, P. Pitchappa, N. Wang, R. Singh, and L. J. Wong, *Advanced Science* **8**, 2100925 (2021).
- [24] P. Zhang, Y. Zhang, and M. Tang, *Opt. Express* **25**, 10901 (2017).
- [25] J. H. Brownell, J. Walsh, and G. Doucas, *Physical Review E* **57**, 1075 (1998).
- [26] J. Giltinan, V. Sridhar, U. Bozuyuk, D. Sheehan, and M. Sitti, *Advanced Intelligent Systems* **3**, 2000204 (2021).
- [27] B. Jian, H. Li, X. He, R. Wang, H. Y. Yang, and Q. Ge, *International Journal of Extreme Manufacturing* **6**, 012001 (2024).
- [28] F. Rothermel, S. Thiele, C. Jung, A. Krapf, S. E. Ilse, B. Merle, H. Giessen, and A. M. Herkommer, *Advanced Materials Technologies* **9**, 2302196 (2024).
- [29] L. Siegle, S. Ristok, and H. Giessen, *Opt. Express* **31**, 4179 (2023).
- [30] F. Mayer *et al.*, *Advanced Materials* **32**, 2002044 (2020).
- [31] V. Hahn, P. Rietz, F. Hermann, P. Müller, C. Barner-Kowollik, T. Schlöder, W. Wenzel, E. Blasco, and M. Wegener, *Nature Photonics* **16**, 784 (2022).
- [32] See Supplemental Material, which includes Refs. [43-45].
- [33] T. Coenen, B. J. M. Brenny, E. J. Vesseur, and A. Polman, *MRS Bulletin* **40**, 359 (2015).
- [34] S. Mignuzzi, M. Mota, T. Coenen, Y. Li, A. P. Mihai, P. K. Petrov, R. F. M. Oulton, S. A. Maier, and R. Sapienza, *ACS Photonics* **5**, 1381 (2018).
- [35] R. Lingstädt, F. Davoodi, K. Elibol, M. Taleb, H. Kwon, P. Fischer, N. Talebi, and P. A. van Aken, *ACS Nano* **17**, 25496 (2023).
- [36] N. Talebi, W. Sigle, R. Vogelgesang, and P. van Aken, *New Journal of Physics* **15**, 053013 (2013).
- [37] J.-F. Zhu, C.-H. Du, Z.-W. Zhang, P.-K. Liu, L. Zhang, and A. W. Cross, *Opt. Lett.* **46**, 4682 (2021).
- [38] L. Jing *et al.*, *Research* **2019** (2019).
- [39] A. R. Neureuther and R. Mittra, *Proceedings of the IEEE* **55**, 2134 (1967).
- [40] K. Mizuno, J. Pae, T. Nozokido, and K. Furuya, *Nature* **328**, 45 (1987).
- [41] N. Talebi, *New Journal of Physics* **18**, 123006 (2016).
- [42] R. Shiloh, J. Illmer, T. Chlouba, P. Yousefi, N. Schönenberger, U. Niedermayer, A. Mittelbach, and P. Hommelhoff, *Nature* **597**, 498 (2021).
- [43] R. F. Harrington, *Time-harmonic electromagnetic fields* (McGraw-Hill Book Company, New York, 1961).
- [44] A. H. Cherin, *Introduction to Optical Fibers* (McGraw-Hill, US, 1982).
- [45] P. B. Johnson and R. W. Christy, *Physical Review B* **6**, 4370 (1972).

Supplementary Information for:

Phase-matched electron-photon interactions enabled with 3D-printed helical waveguides

Masoud Taleb,¹ Mohsen Samadi,² and Nahid Talebi^{1,*}

¹Institute of Experimental and Applied Physics, Kiel University, 24098 Kiel, Germany

²Department of Electrical and Information Engineering, Kiel University, 24143Kiel, Germany

Content:

- 1- Optical modes of the polymer/gold fiber
- 2- Images of the helical waveguide and sample holder
- 3- Dependence of the emission wavelength on the electron's kinetic energy

1- Optical modes of the polymer/gold fiber

To construct the optical modes of the system, we employ the vector potential approach in the cylindrical coordinate system, with ρ , φ , and z being the radius in xy -plane, azimuthal angle, and the z -axis respectively [1]. Optical modes in fibers exhibit a hybrid nature; that is, the modes are not purely transverse except when $n=0$, where n represents the azimuthal degree of freedom [2]. The fiber is composed of a polymer core with the permittivity $\varepsilon_{r1} = 2.63$ within the region specified by $\rho < a$ and a gold thin cladding with the permittivity ε_{r2} [3] within the region $a < \rho < b$, whereas the region $\rho > b$ is considered to be vacuum with $\varepsilon_{r3} = 1$. The solution Ansatz constitutes spatial distributions of the magnetic vector potential, as

$$A_z = \begin{cases} C_1 I_n(\kappa_1 \rho) e^{in\varphi} e^{-ik_z z} & \rho < a \\ (C_2 I_n(\kappa_2 \rho) + C_3 K_n(\kappa_2 \rho)) e^{in\varphi} e^{-ik_z z} & a < \rho < b, \\ C_4 K_n(\kappa_3 \rho) e^{in\varphi} e^{-ik_z z} & \rho > b \end{cases} \quad (\text{S1})$$

and the electric vector potential, as

$$F_z = \begin{cases} D_1 I_n(\kappa_1 \rho) e^{in\varphi} e^{-ik_z z} & \rho < a \\ (D_2 I_n(\kappa_2 \rho) + D_3 K_n(\kappa_2 \rho)) e^{in\varphi} e^{-ik_z z} & a < \rho < b, \\ D_4 K_n(\kappa_3 \rho) e^{in\varphi} e^{-ik_z z} & \rho > b \end{cases} \quad (\text{S2})$$

where C_i and D_i are unknown coefficients to be obtained via satisfying the boundary conditions. k_z is the propagation constant of the waves propagating along the z -axis, and the characteristic equations in all three regions are $-\kappa_i^2 + k_z^2 = \varepsilon_{ri} k_0^2$, with $i = 1, 2$, and 3 . I_n and K_n are the modified Bessel functions of the first and second kinds with order n .

The electric and magnetic field coefficients are obtained as

$$\vec{E}(\vec{r}) = -\vec{\nabla} \times \vec{F} + (i\omega\varepsilon_0\varepsilon_r)^{-1}(\vec{\nabla} \times \vec{\nabla} \times \vec{A}) \quad (\text{S3})$$

and

$$\vec{H}(\vec{r}) = +\vec{\nabla} \times \vec{A} + (i\omega\mu_0)^{-1}(\vec{\nabla} \times \vec{\nabla} \times \vec{F}), \quad (\text{S4})$$

Respectively, with both \vec{A} and \vec{F} vectors composed of only z-components. After obtaining the field coefficients by using equations (S1) to (S2), the tangential boundary conditions are satisfied, and therefore the following 4 coupled equations are obtained that relates C_2 , C_3 , D_2 , and D_3 as

$$\begin{aligned} & + [\kappa_2^2 - \kappa_1^2] \frac{1}{i\omega\varepsilon_0\varepsilon_{r2}} \frac{nk_z}{a} I_n(\kappa_2 a) I_n(\kappa_1 a) C_2 + [\kappa_2^2 - \kappa_1^2] \frac{1}{i\omega\varepsilon_0\varepsilon_{r2}} \frac{nk_z}{a} K_n(\kappa_2 a) I_n(\kappa_1 a) C_3 \\ & + \kappa_1 \kappa_2 \left\{ \kappa_2 I_n'(\kappa_1 a) I_n(\kappa_2 a) - \kappa_1 I_n'(\kappa_2 a) I_n(\kappa_1 a) \right\} D_2 \\ & + \kappa_1 \kappa_2 \left\{ \kappa_2 I_n'(\kappa_1 a) K_n(\kappa_2 a) - \kappa_1 K_n'(\kappa_2 a) I_n(\kappa_1 a) \right\} D_3 = 0, \end{aligned} \quad (\text{S5})$$

$$\begin{aligned} & + [\kappa_2^2 - \kappa_3^2] \frac{1}{i\omega\varepsilon_0\varepsilon_{r2}} \frac{nk_z}{b} I_n(\kappa_2 b) K_n(\kappa_3 b) C_2 + [\kappa_2^2 - \kappa_3^2] \frac{1}{i\omega\varepsilon_0\varepsilon_{r2}} \frac{nk_z}{b} K_n(\kappa_2 b) K_n(\kappa_3 b) C_3 \\ & + \kappa_2 \kappa_3 \left[\kappa_2 K_n'(\kappa_3 b) I_n(\kappa_2 b) - \kappa_3 I_n'(\kappa_2 b) K_n(\kappa_3 b) \right] D_2 \\ & + \kappa_2 \kappa_3 \left[\kappa_2 K_n'(\kappa_3 b) K_n(\kappa_2 b) - \kappa_3 K_n'(\kappa_2 b) K_n(\kappa_3 b) \right] D_3 = 0, \end{aligned} \quad (\text{S6})$$

$$\begin{aligned} & \kappa_1 \kappa_2 \left[-\frac{\varepsilon_{r1}}{\varepsilon_{r2}} \kappa_2 I_n'(\kappa_1 a) I_n(\kappa_2 a) + \kappa_1 I_n'(\kappa_2 a) I_n(\kappa_1 a) \right] C_2 \\ & + \kappa_1 \kappa_2 \left[-\frac{\varepsilon_{r1}}{\varepsilon_{r2}} \kappa_2 I_n'(\kappa_1 a) K_n(\kappa_2 a) + \kappa_1 K_n'(\kappa_2 a) I_n(\kappa_1 a) \right] C_3 \\ & + [\kappa_2^2 - \kappa_1^2] \frac{1}{i\omega\mu_0} \frac{nk_z}{a} I_n(\kappa_2 a) I_n(\kappa_1 a) D_2 + [\kappa_2^2 - \kappa_1^2] \frac{1}{i\omega\mu_0} \frac{nk_z}{a} K_n(\kappa_2 a) I_n(\kappa_1 a) D_3 = 0, \end{aligned} \quad (\text{S7})$$

and

$$\begin{aligned} & \kappa_2 \kappa_3 \left[-\frac{\varepsilon_{r3}}{\varepsilon_{r2}} \kappa_2 K_n'(\kappa_3 b) I_n(\kappa_2 b) + \kappa_3 I_n'(\kappa_2 b) K_n(\kappa_3 b) \right] C_2 \\ & + \kappa_2 \kappa_3 \left[-\frac{\varepsilon_{r3}}{\varepsilon_{r2}} \kappa_2 K_n'(\kappa_3 b) K_n(\kappa_2 b) + \kappa_3 K_n'(\kappa_2 b) K_n(\kappa_3 b) \right] C_3 \\ & + [\kappa_2^2 - \kappa_3^2] \frac{1}{i\omega\mu_0} \frac{nk_z}{b} I_n(\kappa_2 b) K_n(\kappa_3 b) D_2 + [\kappa_2^2 - \kappa_3^2] \frac{1}{i\omega\mu_0} \frac{nk_z}{b} K_n(\kappa_2 b) K_n(\kappa_3 b) D_3 = 0. \end{aligned} \quad (\text{S8})$$

Equations (S5) to (S8) defines a nonlinear Eigenvalue problem, for obtaining the propagation constant k_z and the eigenvectors C_2 , C_3 , D_2 , and D_3 . The unknown coefficients C_1 , C_4 , D_1 , and D_4 are obtained as

$$C_1 = + \frac{\varepsilon_{r1}}{\varepsilon_{r2}} \frac{\kappa_2^2}{\kappa_1^2} \frac{I_n(\kappa_2 a)}{I_n(\kappa_1 a)} C_2 + \frac{\varepsilon_{r1}}{\varepsilon_{r2}} \frac{\kappa_2^2}{\kappa_1^2} \frac{K_n(\kappa_2 a)}{I_n(\kappa_1 a)} C_3, \quad (\text{S9})$$

$$C_4 = +\frac{\varepsilon_{r3} \kappa_2^2 I_n(\kappa_2 b)}{\varepsilon_{r2} \kappa_3^2 K_n(\kappa_3 b)} C_2 + \frac{\varepsilon_{r3} \kappa_2^2 K_n(\kappa_2 b)}{\varepsilon_{r2} \kappa_3^2 K_n(\kappa_3 b)} C_3, \quad (\text{S10})$$

$$D_1 = +D_2 \frac{\kappa_2^2 I_n(\kappa_2 a)}{\kappa_1^2 I_n(\kappa_1 a)} + D_3 \frac{\kappa_2^2 K_n(\kappa_2 a)}{\kappa_1^2 I_n(\kappa_1 a)}, \quad (\text{S11})$$

and

$$D_4 = +D_2 \frac{\kappa_2^2 I_n(\kappa_2 b)}{\kappa_3^2 K_n(\kappa_3 b)} + D_3 \frac{\kappa_2^2 K_n(\kappa_2 b)}{\kappa_3^2 K_n(\kappa_3 b)},$$

Which are used to calculate the spatial distribution of the electric and magnetic fields in all regions.

2. Images of the helical waveguide and sample holder

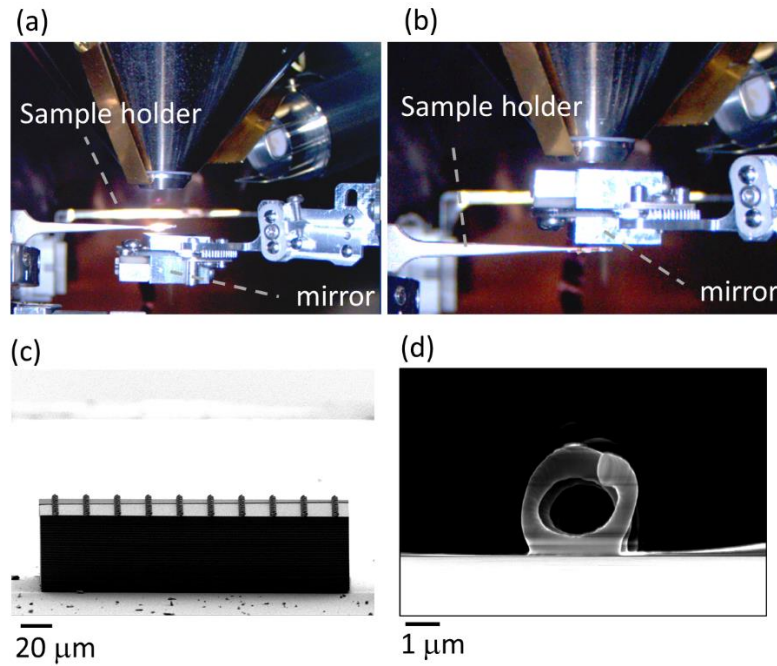


FIG. S1. (a) The setup, consisting of a sample holder inside a scanning electron microscope and a parabolic mirror positioned below the sample. (b) The same setup with the parabolic mirror positioned above the sample. (c) A scanning electron (SE) image of the sample, showing a series of microhelices arranged on top of a plateau. (d) A high-magnification top-view image of a single helix, demonstrating the alignment of the helix axis parallel to the electron trajectory.

3. Dependence of the emission wavelength on the electron's kinetic energy

The phase-matching condition defined in Eq. (1) of the main text enables control over the photon energy and intensity for a specific helix through various parameters, including the electron's group velocity and the diffraction order m . Fig. S2 illustrates that the emitted photon energy is indeed dependent on the electron's kinetic energy. For an electron with the kinetic energy of 15 keV ($v_e = 0.24c$, where c is the light speed in vacuum), only a faint emission is observed, which is two orders of magnitude weaker than the emission from a 17 keV electron beam. For the latter, the emission occurs at the peak photon energy of $E = 2.2$ eV, in a good agreement with the phase-matching condition. For an electron beam with the kinetic energy of 20 keV ($v_e = 0.27c$), the peak photon energy occurs at $E = 2.4$ eV, whereas the phase-matching condition specifies an emission at the energy of 2.65 eV. The emission angle is higher than that observed for an electron with a kinetic energy of 17 keV. Both observations indicate that the emission corresponds to the $m = 1$ diffraction order. This condition results in an emission at a photon energy of 2.5 eV, which aligns better with the experimental observations.

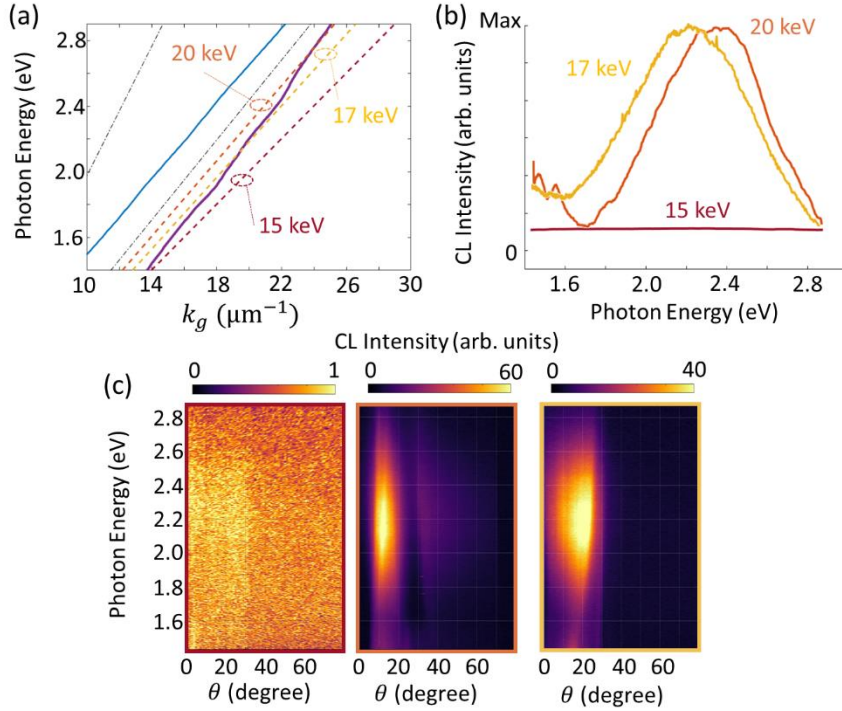


FIG. S2. (a) Dispersion diagram of the fundamental mode (Solid purple line) and the second mode (solid blue line) of the optical fiber. Dashed-dotted lines display the optical lines in vacuum and in the polymer. The colored dashed lines exhibit the phase-matching condition for an electron with depicted kinetic energies propagating parallel to the helix axis. (b) CL spectra and (b) CL angle-resolved spectral maps for an electron with the kinetic energies of 15 keV (left), 17 keV (middle), and 20 keV (right) propagating parallel to the helix.